CHEMISTRY OF MATERIALS

pubs.acs.org/cm Article

Direct Observation of Electron Beam-Induced Phase Transition in $MgCrMnO_4$

Prakash Parajuli,*,⊥ Haesun Park,⊥ Bob Jin Kwon, Jinglong Guo, Baris Key, John T. Vaughey, Peter Zapol, and Robert F. Klie*

Cite This: *Chem. Mater.* 2020, 32, 10456–10462 Read Online

ACCESS | Metrics & More | Article Recommendations | Supporting Information

ABSTRACT: Irreversible structural transformation in intercalation-type cathode materials, which has been frequently observed, has been perceived as a principal cause of capacity fading and voltage decay in (uni) multivalent batteries. Herein, we explored the electron beam-induced spinel to defective rocksalt phase transitions in $MgCrMnO_4$, a potential multivalent cation intercalation cathode, using atomic-resolution imaging and spectroscopy in an aberration-corrected scanning transmission electron microscope. This dynamic electron beam irradiation study of specific structural transformations provides an atomistic understanding of the structural evolution observed in transition-metal oxide spinels during electrochemical cycling using multivalent cations, such as Mg^{2+}. By combining an imaging study with first-principles modeling, we demonstrate that the mechanism of the spinel to defective rocksalt transformation in $MgCrMnO_4$ nanostructures is enabled by the presence of oxygen vacancies and is, therefore, very similar to that observed in transition-metal oxide spinels upon Li intercalation.

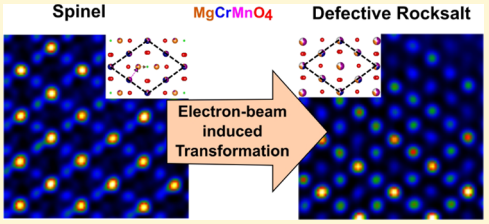

INTRODUCTION

Transition-metal (TM) oxide spinels, particularly manganese oxide compounds, are receiving significant interest in the rechargeable battery community because of their potential use as hosts for multivalent ion intercalation. These materials provide three-dimensional pathways of cation migration and offer a diversity of favorable intercalation sites.[1] For reversible electrochemical cyclability, cathode materials are expected to retain their structural frameworks during cation insertion and extraction. However, in the Li-ion community, many studies have shown that during electrochemical cycling of TM oxides, new structures or phases are formed, ultimately leading to the capacity fading or voltage decay.[2] Particularly, the phase transition between layered, spinel, and rocksalt structures has been frequently observed in the manganese-containing cathodes.[2−7] Numerous studies suggested that structural transformations, especially at the particle surfaces, are a consequence of the migration of the cations and the creation of oxygen vacancies causing the reduction in the energy barriers for cation migration.[5,8,9]

Using TM oxides as cathodes for multivalent ion intercalation, such as Mg^{2+} or Ca^{2+}, is still relatively new, and there are only a limited number of studies reporting reversible Mg cycling.[10−13] Interestingly, imaging studies of cycled multivalent cathodes based on TM spinels exhibit a structural transformation on the particle surfaces that is similar to that observed in the Li-ion counterpart. Despite extensive studies on the reconstructed structures in Li-ion cathode materials, various aspects of these phase transformations, including the TM cation migration pathways, intermediate states, migration length, and atomic and electronic structures of phase boundaries, lack detailed understanding. Revealing these details dynamically during structural changes is crucial for elucidating the behavior of reversible intercalation in multivalent batteries.

In this study, we perform electron microscopy experiments and first-principles calculations to explore the dynamics of phase transition from spinel to rocksalt in $MgCrMnO_4$. The particles are exposed to an intense electron beam (an approximate dose of 10^7 $e^-/Å^2$) and both the structural and electronic changes induced by the electron beam are investigated through atomic-resolution imaging and electron energy loss spectroscopy (EELS). Although electron irradiation is not a substitute for electrochemical cycling, various details can be learned from the structural and electronic changes induced by the procedure.[8] We use the electron beam irradiation to accelerate structural transformations while simultaneously obtaining real-time microscopy and spectroscopy information on specific oxide particles at atomic resolution. This technique has already been widely used to explore the phase transition[9,14−18] and dynamics of single

Received: July 29, 2020
Revised: November 11, 2020
Published: November 30, 2020

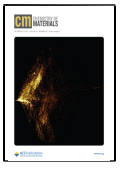

https://dx.doi.org/10.1021/acs.chemmater.0c03121
Chem. Mater. 2020, 32, 10456−10462

dopant and defects motion[19,20] in a variety of materials. First-principles calculations are performed to get insight into the Mg/Mn migration behavior in the presence of defects.

METHODS

$MgCrMnO_4$ nanocrystals were synthesized by an aqueous sol−gel reaction using magnesium acetate tetrahydrate, chromium acetate hydroxide, manganese acetate dihydrate as a precursor and citric acid as a capping agent. Details about synthesis can be found elsewhere.[21] Magnesium, chromium, and manganese were homogeneously distributed with a stoichiometric ratio throughout the nanocrystalline particles, confirming the presence of a solid solution (Figure S1).

Scanning transmission electron microscopy (STEM) imaging, energy-dispersive X-ray (EDX) and electron energy loss (EEL) spectroscopy were performed on an aberration-corrected JEOL JEM-ARM200CF, equipped with a cold field emission and operated at 200 kV, which allows ∼73 pm spatial resolution and ∼0.35 eV energy resolution. High-angle annular dark-field (HAADF) images were acquired using a convergence semiangle of 23 mrad and a collection angle from 90 to 175 mrad. EDX spectra were collected by an Oxford X-max 100TLE windowless silicon drift EDX detector, and EEL spectra were collected using the Gatan Quantum imaging filter with a convergence angle of 30 mrad and a collection angle of 35 mrad. The probe current was approx. 19 and 62 pA during the acquisition of images and EELS spectra, respectively. HAADF image simulation was performed using μSTEM software package.[22]

The migration energies of Mg and Mn cations were calculated by the density functional theory (DFT)[23] method, as implemented in the Vienna ab initio simulation package (VASP).[24] The projector-augmented wave (PAW)[25,26] potentials were used and the plane-wave cutoff energy was set to 520 eV. The generalized gradient approximation (GGA) formulated by Perdew−Burke−Ernzerhof (PBE) was used to describe the exchange-correlation functional.[27] The single-ionic migration barriers are calculated by means of the nudged elastic band (NEB) method.[28] The simulation cells for NEB consisted of a supercell generated from a 2 × 2 × 2 of the $MgCrMnO_4$ unit cell. The $MgCrMnO_4$ unit cell was adopted from the previous study.[21] The observed 16% site inversion between Mg (8a) and Mn (16d)[21] was modeled by swapping the positions of three Mn and Mg atoms in a 2 × 2 × 2 of the normal spinel unit cell, resulting in 18% Mn/Mg site inversion. The *k*-point mesh of 2 × 2 × 2 was used for the NEB calculations, and the atom positions were relaxed to the atomic force tolerance of 0.05 eV/Å.

RESULTS AND DISCUSSION

Atomic-resolution HAADF images of the $MgCrMnO_4$ nanostructure are summarized in Figure 1. To follow the effects of beam irradiation, images of the exact same area (marked by a rectangle in Figure 1a) of the particle were scanned (approx. dose 10^7 e/Å^2) two times and then another image, Figure 1a, was captured at slightly reduced magnification to show both the irradiated and neighboring pristine regions of the particle. Figure 1b,c shows the image of the same area of the particle before and after electron beam irradiation. Close examination of the images shows that the image taken at the second time is significantly different from that taken at the first scan. This is evident in the comparison of the regions I and II in Figure 1a as well.

The first image of the particle shows a spinel structure containing a diamond-shaped pattern (a model of the structure is shown as an inset in Figure 1b) of the alternative bright and less bright columns along the edge of the rhombus and least bright columns inside the rhombus. Since the spinel structure contains an uneven number density of atoms at different sites of the structure, elemental identification through the HAADF image was not straightforward, despite the fact that the

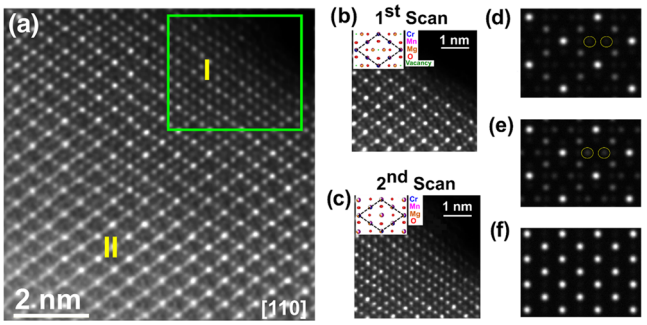

Figure 1. Filtered HAADF images of the $MgCrMnO_4$ nanostructure before and after structural transformation. (a) Atomic-level image showing two distinct phases: region II-spinel phase (before structural transformation) and region I-rocksalt phase (after transformation). (b, c) Image of the particle (marked by the rectangle in (a)) in first and second scans, respectively, showing structural transformation from spinel to rocksalt, inset: corresponding models. (d−f) HAADF simulated images of normal spinel, defective spinel, and rocksalt structure, respectively.

contrast in HAADF images is approximately proportional to the square of the average atomic number of the illuminated column.[29] For more quantitative analysis, we performed a multislice image simulation. Two different configurations for HAADF simulation were considered, the normal spinel—Cr/Mn at 16d site and Mg at 8a site, as well as a defective spinel structure in which 8a and 16d sites are occupied by both Mg and Mn cations following the crystal structure reported in the earlier studies.[21] Atomic sites in the crystal are denoted based on Wyckoff notation.[30] The Mg columns at the tetrahedral sites (marked by the yellow circles) are not differentiable in the normal spinel structure (Figure 1d); this is not surprising, provided that the intensity of heavy neighboring elements (Mn and Cr) is predominantly high. On the other hand, distinct atomic contrast corresponding to the cations can be seen in the disordered spinel structure (Figure 1e), indicating the presence of higher atomic number elements at tetrahedral sites. This suggests that not only Mg cations but also Mn cations occupy the 8a sites. This agreed to the previously reported results claiming Mg/Mn inversion in various manganese oxide compounds.[21,31−33]

The HAADF image of the particle after the second scan (Figure 1c) is significantly different than the experimental spinel structure as well as the simulated defective spinel structure. In particular, the intensity of the atomic columns no longer resembled a differential contrast diamond-shaped structure. This indicates that the spinel structure is altered by electron irradiation. The new structure lacks atoms on the tetrahedral 8a sites (occupied in spinel structure), and new atomic columns appeared at the 16c site, which was empty in the spinel structure. Furthermore, the contrast of the atomic columns corresponding to the new structure is approximately uniform, indicating that the crystal structure is more symmetric, and the unit cell is half of the diamond-shaped spinel unit cell. Considering the observation, we simulated a HAADF image of the defective rocksalt structure, Cr, Mg/Mn at 16d sites and that of Mg/Mn at the 16c site (Figure 1e). In fact, the simulated image for the defective rocksalt structure matches the experimental image. Hence, this suggests that the new structure is the rocksalt phase.

In addition to tracking the atomic position of the cations, EEL spectra were obtained from the pristine and irradiated

https://dx.doi.org/10.1021/acs.chemmater.0c03121
Chem. Mater. 2020, 32, 10456−10462

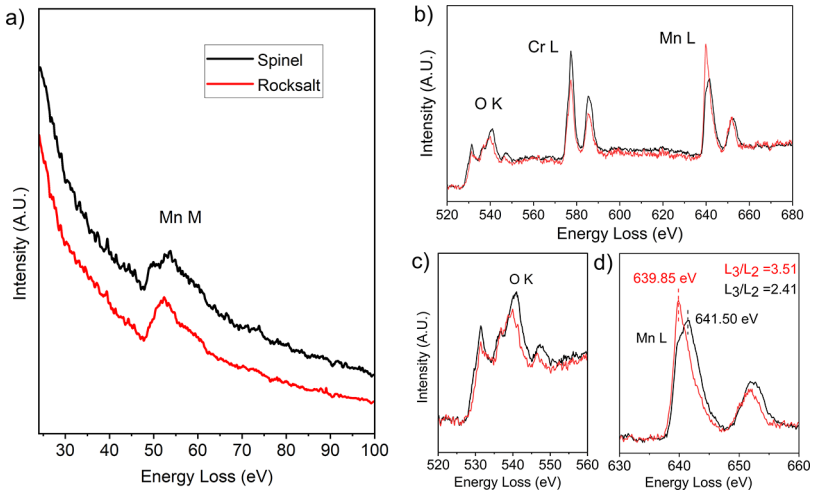

Figure 2. Electron energy loss spectroscopy analysis of the $MgCrMnO_4$ nanostructure before and after structural transformation. (a) Low-loss spectra showing Mn *M*-edge, (b) core-loss spectra showing O *K*-, Cr *L*-, and Mn *L*-edges. Expended views of O *K*- and Mn *L*-edges are shown in (c) and (d). The spectra in black and red represent spinel and rocksalt phases, respectively.

regions to monitor potential changes in the composition, the transition-metal valence states, and the evolutions of chemical environments (Figure 2) upon the observed phase transition. The two spectra shown in Figure 2 were acquired from the pristine spinel and defective rocksalt structures at the surface of particles. The Mn *M*-edge has an energy onset of 51 eV and has been used in $LiMn_2O_4$ spinels to track the presence of rocksalt phases.[9] The Mn *M*-edge (Figure 2a) shows a prominent prepeak at 51 eV for the spinel structure, which disappears in the spectra taken from a rocksalt region. A decrease in the prepeak intensity has been associated with the change in the concentration of Mn on the octahedral sites. Specifically, the prepeak intensity is proportional to the concentration of Mn at the 16d sites, which is reduced when Mn migrates from the 16d octahedral to the 16c octahedral sites. Our results are in agreement with prior studies showing rocksalt phases in LMO materials.[9]

Figure 2b shows core-loss spectra of the O *K*-, Cr *L*-, and Mn *L*-edges. The energy scales are calibrated with respect to the zero-loss peak and the background is removed by a power-law fitting. The O *K*- and TM *L*-edges can be used to track changes to both the O content and TM valence states. Specifically, the O *K*-edge prepeak probe transitions from the 1s into the hybridized O 2p−TM 3d orbitals,[34] and thus the intensity ratio of O *K*-edge prepeak to the total O *K*-edge intensity (hereafter referred as the O prepeak intensity) will generally decrease with decreasing oxygen concentration and valence states of TM. Additionally, the energy onset of TM L_3-edge, the intensity ratio of L_3 and L_2 white lines of TM (hereafter referred as the L_3/L_2 ratio), and separation of *L*-edges are also a strong indication of the TM valence, with high-energy chemical shifts, and decreasing intensity ratios and *L*-edges separation corresponding to an increase in valance state.[35−39] Meticulous observation of core-loss EEL spectra acquired from the newly created defective rocksalt structure and the neighboring spinel structure clearly shows the change in chemical environment due to the beam irradiation. The changes in the O *K*- as well as Mn *L*-edges (expanded view in Figure 2c,d) are visible and will be discussed below; we note that there is no change in the Cr *L*-edge. The Cr *L*-edge onset and L_3/L_2 ratio remain unchanged in the two regions, suggesting that Cr does not participate effectively in this phase transition.

Figure 2c shows the oxygen *K*-edge spectra obtained from the pristine and transformed regions of the sample. The spectra are normalized to the Mn L_3 peak intensity. When comparing the spectra, an increase in O prepeak intensity (spinel: 0.2971 and rocksalt: 0.3261) is observed, indicating the decrease in oxygen concentration as well as the Mn valance state.[8] This is further validated by EELS quantification, computed using core-loss spectrum containing O *K*-, Cr-*L* and Mn *L*-edges (Figure 2b), which shows approximately 2% oxygen loss during the phase transition. In addition, the Mn *L*-edges (Figure 2d) extracted from the transformed structure show an energy shift toward lower energy as well as an increase in the separation of the Mn *L*-edges. We also find an increase in the Mn L_3/L_2 intensity ratio, reflecting a decrease of the Mn valence. Quantitative values of all of the EELS results are summarized in Table 1. Furthermore, Mn *L*-edges spectra show two notable features: a left shoulder on the Mn L_3-peak for spinel structure and the disappearance of the spinel main peak and growth of the shoulder into the main peak in the rocksalt structure. The left shoulder of the Mn L_3-peak on spinel structure indicates the presence of a small fraction of the rocksalt phase,[3] which is not unexpected given that the specimen had already experienced a significant dose during imaging and EEL acquisition, which grows and forms a prominent peak after structural transformation in the defective rocksalt phase.

Table 1. Comparison of Mn *L*-Edges Peak Position, Energy Separation, and Intensity Ratios of Pristine and Transformed Materials

stage	Mn L_3 peak energy (eV)	ΔE ($L_3 - L_2$) (eV)	intensity ratio (L_3/L_2)	oxidation state
pristine (spinel)	641.50	10.87	2.41	3.00+
transformed (defective rocksalt)	639.85	11.83	3.51	2.25+

Various procedures, such as the white-line intensity ratio, chemical shift of TM L_3-edge, O *K*- edge onset, and edge onset differences (TM *L*-edges and O *K*-edges), are used to link the

https://dx.doi.org/10.1021/acs.chemmater.0c03121
Chem. Mater. 2020, 32, 10456−10462

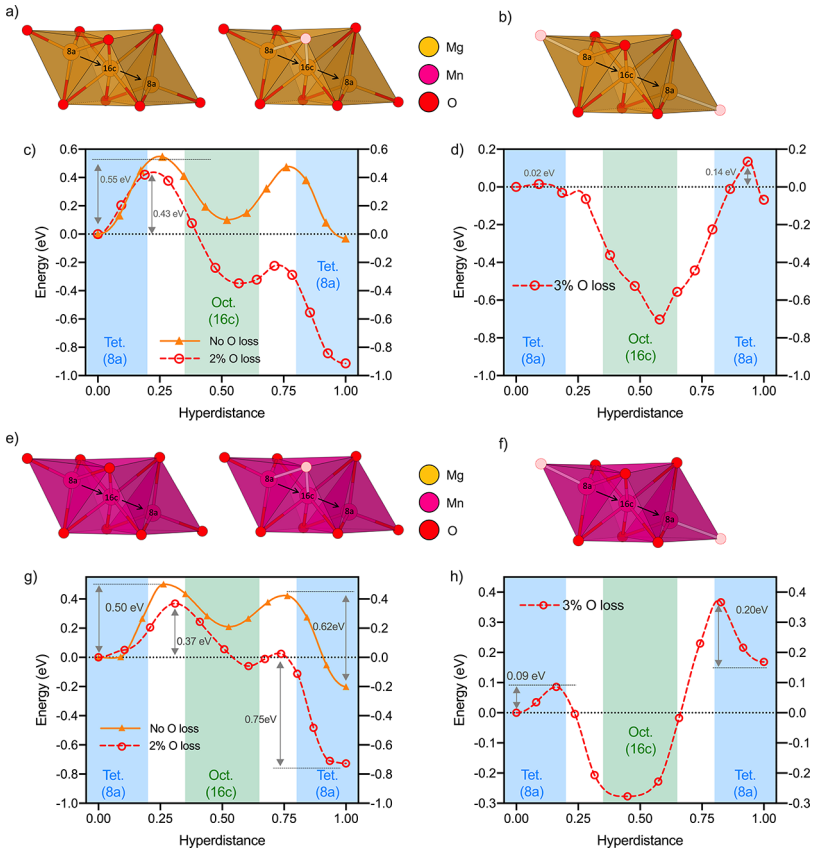

Figure 3. Pathways and energies of cation hopping between tetrahedral 8a sites through an octahedral 16c site in the 18% Mg/Mn inverted $MgCrMnO_4$ spinel. The (a, b) Mg and (e, f) Mn migration pathways are depicted using ball and stick models. The yellow, magenta, and red spheres represent Mg, Mn, and O atoms. The hatched red sphere signifies a single O vacancy in the periodic cell. The minimum energy pathways (MEPs) for (c, d) Mg migration and (g, h) Mn migration are shown. The solid-orange and dashed-red lines represent the MEPs without and with O loss, respectively. The shaded areas convey the information of approximate coordination environments of cations along the MEPs; blue: tetrahedra, green: octahedra.

EELS fine-structures to the oxidation states of the TM oxides.[40] Among these, the most popular and common method to relate EELS spectra to the oxidation state is the white-line intensity ratio. Even though the interpretation of these results varies widely,[8,36−39,41,42] numerous studies employed the Mn L_3/L_2-ratio to determine the Mn valence. Minimal variation in the EELS data is expected, given that the chemical environment of the Mn atoms varies in different studies, in addition to the electron microscopy acquisition parameters corresponding to the EEL spectra. Our results of the pristine structure show a Mn L_3/L_2-ratio and separation of Mn L-edges that are in agreement with prior studies of Mn^{3+}.[36,42] In the defective rocksalt structure, we find that the Mn L_3/L_2 ratio and separation of Mn L-edges indicate the presence of $Mn^{2.25+}$ valence state.

To gain insight into the cation migration during this observed phase transition, first-principles calculations were performed (Figures 3, 4, and S2). Previous first-principles calculations suggest relatively low migration barriers for Mg ions in the $MgMn_2O_4$ spinel phase that could be either increased or lowered by spinel inversion.[43] The results for the migration pathways and energies of the Mg and Mn cations, in partially inverted (18% Mg/Mn inversion) stoichiometric and 2% oxygen-deficient spinel $MgCrMnO_4$ structures, are shown in Figure 3. The calculated energy barriers for Mg and Mn cations to hop from a tetrahedral 8a to an octahedral 16c site are 0.55 and 0.50 eV, respectively, for the stochiometric partially inverted structure. These energy barriers reduce to 0.45 and 0.37 eV, respectively, in oxygen-deficient materials when the migrating cation moves away from the oxygen vacancy, due to a strong attractive interaction between cation and anion vacancies. For comparison, the Mg/Mn energy pathways were calculated in the normal spinel structure (shown in Figure S2) and our results show similar behavior to the partially inverted spinel structure, decrease in both the migration barrier (from 0.55 to 0.33 eV). However, migration of Mg and Mn cations toward oxygen vacancy has higher barriers, over 1 eV. The lowest-energy positions of cations along the pathway can be either 8a or 16c, dependent on the specific distribution of the oxygen vacancies, as shown in Figure 3. Previous reports on electron beam-induced damage in oxides[44] and, more specifically, in electron irradiation-induced transition of Mn_3O_4 spinel to MnO rocksalt structures[45] indicate that O ions can be moved by the electric field due to charge layers on the surface produced by the irradiation, contributing to the phase transformation. Our calculations show that migration of the cations is related to the oxygen migration due to strong attractive interactions between oxygen vacancies and Mg/Mn vacancies in oxygen-deficient spinel structure. Therefore, oxygen loss results in faster Mg/Mn cation diffusion, facilitating the phase transition in the surface region. These results imply that additional energy is needed to overcome these Mg/Mn migration barriers leading to the spinel to the defective rocksalt phase transition. In the

https://dx.doi.org/10.1021/acs.chemmater.0c03121
Chem. Mater. 2020, 32, 10456−10462

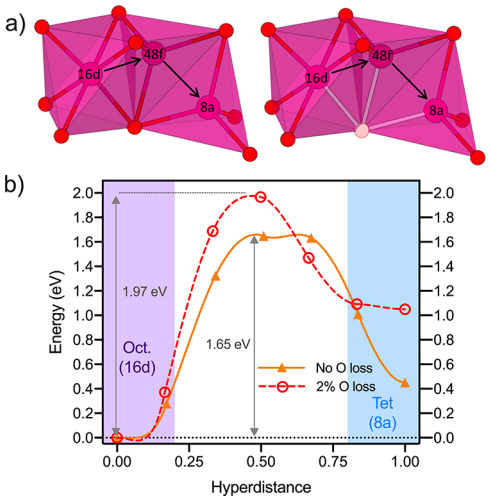

Figure 4. Mn migration pathway and energies from an octahedral 16d site to a tetrahedral 8a site through a tetrahedral 48f site in the 18% Mg/Mn inverted $MgCrMnO_4$ spinel. (a) Mn migration pathways are depicted using ball and stick models. The magenta and red spheres represent Mn and O atoms. The hatched red sphere signifies a single O vacancy in the periodic cell, which corresponds to a 2% O loss. The minimum energy pathways (MEPs) for (b) Mn migration are shown. The solid-orange and dashed-red lines represent the MEPs without and with 2% O loss, respectively. The shaded areas convey the information of approximate coordination environments of cations along the MEPs; blue: tetrahedra, purple: octahedra.

dynamic electron beam irradiation experiments shown here, this energy is provided by the scattering due to the impinging high-energy electron beam,[46] whereas in the electrochemical experiments reported earlier,[21] the electrochemical potential during the charge−discharge cycles provided this energy, and this migration process is further accelerated by the presence or creation of oxygen vacancies during the charge−discharge cycles.

Similarly, we explored the Mn migration from octahedral 16d sites to tetrahedral 8a sites (Figures 4 and S2). Both the configuration energy and energy barrier show that the Mn migration from 16d to 8a sites is not energetically feasible in either stoichiometric or oxygen-deficient materials. However, the experimental results clearly reveal Mn migration into the 16c site. We infer this as a complex behavior of the Mn migration in a newly formed chemical environment, caused by the alteration in bonding and stoichiometry during structural transformation. Similar structural evolution and impacts on both the configuration energy and the barrier for cation diffusion during external excitations (electrochemical cycling/electron beam irradiation experiment) have been reported in Li containing TM oxides.[47,48]

Close observation of the atomic structure of spinel TM oxides shows two possible pathways for Mn migration from 16d to 16c sites: direct migration from 16d to the empty octahedral site ($Mn_{(oct\text{-}16d)}\rightarrow Mn_{(oct\text{-}16c)}$) or via neighboring tetrahedral site ($Mn_{(oct\text{-}16d)}\rightarrow Mn_{(tet\text{-}8a)}\rightarrow Mn_{(oct\text{-}16c)}$). Although Mn is octahedrally coordinated in both sites, the later pathway via the tetrahedral site is more preferred due to the lower repulsive forces between cations and oxygen along the way. The direct migration from 16d to 16c requires emptying two nearby 8a sites; otherwise, strong repulsion between cations in 16d and 8a induces a large energy penalty. Leaving two 8a sites vacant is equivalent to a 12.5% vacancy concentration, which does not correctly mimic the experimental setup. A previous study, although the condition is not exactly consistent with our study, has shown that the energy for migration of Cr from the 16d site to 16c site in $Mg_{0.67}Cr_2O_4$ spinel is greater than 2 eV, which in part supports our hypothesis that the 16d→16c path is unfavorable. Furthermore, as illustrated in Figure 3, the second step of the pathway: $Mn_{(tet\text{-}8a)}\rightarrow Mn_{(oct\text{-}16c)}$ is energetically favorable in oxygen-deficient materials. Hence, despite some discrepancies with the former step in the Mn migration pathway, we conclude that the Mn migration most likely occurs via the neighboring tetrahedral site ($Mn_{(oct\text{-}16d)}\rightarrow Mn_{(tet\text{-}8a)}\rightarrow Mn_{(oct\text{-}16c)}$) during phase transition, in agreement with earlier reports for TM migration in oxide spinels.[5,7,9] Herein, $MgCrMnO_4$ rapidly transformed into rocksalt phase, hence, the evolution of Mn in tetrahedral sites was not possible to track explicitly, more in-depth analysis of the Mn migration pathways spanning numerous spinel materials will be reported in a future publication.

CONCLUSIONS

In summary, electron beam irradiation and first-principles calculations have been used to induce and study phase transitions in a solid-solution $MgCrMnO_4$ nanoparticle. The evolution of structural and electronic properties is explored in detail, confirming that the spinel $MgCrMnO_4$ transforms into a defective rocksalt structure near the surface of cathode nanoparticles. This transformation occurs via cation (Mg/Mn) migration, facilitated by the creation of oxygen vacancies, and requires additional energy input provided by the electron beam or electrochemical potential to reduce the difference in free energies of the phases and overcome kinetic barriers for cation diffusion. The conclusions of this study are relevant to both the broader battery and electron microscopy communities. Structural transformations due to the TM diffusion are a general issue for cathode materials, and we provide an atomic-scale understanding of how this transformation occurs in transition-metal oxide spinels used for multivalent ion intercalation. We track this transformation on the same location within the particle using dynamic electron beam irradiation, something that is not possible during ex-situ electrochemical cycling experiments. Furthermore, the crystal structure transformation induced by the electron beam reproduces the effects seen in the cathodes that have been cycled for Mg-ion batteries. Therefore, understanding the pathways and energetics of the observed phase transformation provides guidelines on how to modify the surfaces of nanoparticle materials used as multivalent battery cathodes. Since oxygen vacancies appear to enable the Mg/Mn inversion and thus the formation of a rocksalt phase, several options should be (re)considered for stabilizing the surface of the particles. Similar to efforts in Li-ion cathodes, the deposition of a thin, more stable epitaxial layer can prevent the dissolution of oxygen into the electrolyte. Moreover, doping the structure with redox-inactive materials could further increase the energy barriers and thereby minimize the formation of an inverted spinel or a rocksalt surface layer.

In conclusion, we have demonstrated that the dynamic electron microscopy experiments mimicking the electrochemical cell provide helpful knowledge and unprecedented opportunities to further strengthen the understanding of the degradation mechanism for electrode materials.

https://dx.doi.org/10.1021/acs.chemmater.0c03121
Chem. Mater. 2020, 32, 10456−10462

■ ASSOCIATED CONTENT

Supporting Information

The Supporting Information is available free of charge at https://pubs.acs.org/doi/10.1021/acs.chemmater.0c03121.

EDS spectroscopy of the $MgCrMnO_4$ nanostructures, the pathways and energies for Mg migration (8a→16c→8a) and Mn migration (16d→48f→16c) in normal spinel (PDF)

■ AUTHOR INFORMATION

Corresponding Authors

Prakash Parajuli − *Department of Physics, University of Illinois at Chicago, Chicago, Illinois 60607, United States; Joint Center for Energy Storage Research (JCESR), Argonne National Laboratory, Lemont, Illinois 60439, United States;* orcid.org/0000-0001-6732-2010; Email: prakashp@uic.edu

Robert F. Klie − *Department of Physics, University of Illinois at Chicago, Chicago, Illinois 60607, United States; Joint Center for Energy Storage Research (JCESR), Argonne National Laboratory, Lemont, Illinois 60439, United States;* orcid.org/0000-0003-4773-6667; Email: rfklie@uic.edu

Authors

Haesun Park − *Joint Center for Energy Storage Research (JCESR) and Materials Science Division, Argonne National Laboratory, Lemont, Illinois 60439, United States;* orcid.org/0000-0001-6266-8151

Bob Jin Kwon − *Joint Center for Energy Storage Research (JCESR) and Chemical Sciences and Engineering Division, Argonne National Laboratory, Lemont, Illinois 60439, United States;* orcid.org/0000-0001-7395-0814

Jinglong Guo − *Department of Physics, University of Illinois at Chicago, Chicago, Illinois 60607, United States*

Baris Key − *Joint Center for Energy Storage Research (JCESR) and Chemical Sciences and Engineering Division, Argonne National Laboratory, Lemont, Illinois 60439, United States;* orcid.org/0000-0002-1987-1629

John T. Vaughey − *Joint Center for Energy Storage Research (JCESR) and Chemical Sciences and Engineering Division, Argonne National Laboratory, Lemont, Illinois 60439, United States;* orcid.org/0000-0002-2556-6129

Peter Zapol − *Joint Center for Energy Storage Research (JCESR) and Chemical Sciences and Engineering Division, Argonne National Laboratory, Lemont, Illinois 60439, United States;* orcid.org/0000-0003-0570-9169

Complete contact information is available at: https://pubs.acs.org/10.1021/acs.chemmater.0c03121

Author Contributions

[⊥]P.P. and H.P. contributed equally to this work.

Notes

The authors declare no competing financial interest.

■ ACKNOWLEDGMENTS

This work is supported by the Joint Center for Energy Storage Research (JCESR), an Energy Innovation Hub funded by the U.S. Department of Energy, Office of Science, Basic Energy Sciences. The work at the Argonne National Laboratory (ANL) was performed under Contract No. DE-AC02-06CH11357. The authors acknowledge grants of computer time from the ANL Laboratory Computing Resource Center. This work made use of instruments in the Electron Microcopy Service, specifically JEOL JEM-ARM200CF in the Research Resources Center, the University of Illinois at Chicago. The acquisition of UIC JEOL JEM-ARM200CF was supported by an MRI-R^2 grant from the National Science Foundation (DMR-0959470) and the upgraded Gatan Continuum spectrometer was supported by a grant from the NSF (DMR-1626065).

■ REFERENCES

(1) Liu, M.; Rong, Z.; Malik, R.; Canepa, P.; Jain, A.; Ceder, G.; Persson, K. A. Spinel Compounds as Multivalent Battery Cathodes: A Systematic Evaluation Based on Ab Initio Calculations. *Energy Environ. Sci.* **2015**, *8*, 964−974.

(2) Mohanty, D.; Li, J.; Abraham, D. P.; Huq, A.; Payzant, E. A.; Wood, D. L., III; Daniel, C. Unraveling the Voltage-Fade Mechanism in High-Energy-Density Lithium-Ion Batteries: Origin of the Tetrahedral Cations for Spinel Conversion. *Chem. Mater.* **2014**, *26*, 6272−6280.

(3) Lin, F.; Markus, I. M.; Nordlund, D.; Weng, T.-C.; Asta, M. D.; Xin, H. L.; Doeff, M. M. Surface Reconstruction and Chemical Evolution of Stoichiometric Layered Cathode Materials for Lithium-Ion Batteries. *Nat. Commun.* **2014**, *5*, No. 3529.

(4) Xu, B.; Fell, C. R.; Chi, M.; Meng, Y. S. Identifying Surface Structural Changes in Layered Li-Excess Nickel Manganese Oxides in High Voltage Lithium Ion Batteries: A Joint Experimental and Theoretical Study. *Energy Environ. Sci.* **2011**, *4*, 2223−2233.

(5) Qian, D.; Xu, B.; Chi, M.; Meng, Y. S. Uncovering the Roles of Oxygen Vacancies in Cation Migration in Lithium Excess Layered Oxides. *Phys. Chem. Chem. Phys.* **2014**, *16*, 14665−14668.

(6) Lin, M.; Ben, L.; Sun, Y.; Wang, H.; Yang, Z.; Gu, L.; Yu, X.; Yang, X.-Q.; Zhao, H.; Yu, R.; et al. Insight into the Atomic Structure of High-Voltage Spinel $LiNi_{0.5}Mn_{1.5}O_4$ Cathode Material in the First Cycle. *Chem. Mater.* **2015**, *27*, 292−303.

(7) Okamoto, N. L.; Shimokawa, K.; Tanimura, H.; Ichitsubo, T. Feasible Transformation of $MgCo_2O_4$ from Spinel to Defect Rocksalt Structure under Electron Irradiation. *Scr. Mater.* **2019**, *167*, 26−30.

(8) Phillips, P. J.; Iddir, H.; Abraham, D. P.; Klie, R. F. Direct Observation of the Structural and Electronic Changes of Li_2MnO_3 during Electron Irradiation. *Appl. Phys. Lett.* **2014**, *105*, No. 113905.

(9) Gao, P.; Ishikawa, R.; Tochigi, E.; Kumamoto, A.; Shibata, N.; Ikuhara, Y. Atomic-Scale Tracking of a Phase Transition from Spinel to Rocksalt in Lithium Manganese Oxide. *Chem. Mater.* **2017**, *29*, 1006−1013.

(10) Sun, X.; Bonnick, P.; Duffort, V.; Liu, M.; Rong, Z.; Persson, K. A.; Ceder, G.; Nazar, L. F. A High Capacity Thiospinel Cathode for Mg Batteries. *Energy Environ. Sci.* **2016**, *9*, 2273−2277.

(11) Aurbach, D.; Lu, Z.; Schechter, A.; Gofer, Y.; Gizbar, H.; Turgeman, R.; Cohen, Y.; Moshkovich, M.; Levi, E. Prototype Systems for Rechargeable Magnesium Batteries. *Nature* **2000**, *407*, 724−727.

(12) Zhao, M.-Q.; Ren, C. E.; Alhabeb, M.; Anasori, B.; Barsoum, M. W.; Gogotsi, Y. Magnesium-Ion Storage Capability of MXenes. *ACS Appl. Energy Mater.* **2019**, *2*, 1572−1578.

(13) Canepa, P.; Sai Gautam, G.; Hannah, D. C.; Malik, R.; Liu, M.; Gallagher, K. G.; Persson, K. A.; Ceder, G. Odyssey of Multivalent Cathode Materials: Open Questions and Future Challenges. *Chem. Rev.* **2017**, *117*, 4287−4341.

(14) Warner, J. H.; Margine, E. R.; Mukai, M.; Robertson, A. W.; Giustino, F.; Kirkland, A. I. Dislocation-Driven Deformations in Graphene. *Science* **2012**, *337*, 209−212.

(15) Lin, Y.-C.; Dumcenco, D. O.; Huang, Y.-S.; Suenaga, K. Atomic Mechanism of the Semiconducting-to-Metallic Phase Transition in Single-Layered MoS_2. *Nat. Nanotechnol.* **2014**, *9*, 391.

(16) Su, D.; Wang, F.; Ma, C.; Jiang, N. Engineering Nano-Composite $Li_4Ti_5O_{12}$ Anodes via Scanning Electron-Probe Fabrication. *Nano Energy* **2013**, *2*, 343−350.

(17) Pennycook, T. J.; Jones, L.; Pettersson, H.; Coelho, J.; Canavan, M.; Mendoza-Sanchez, B.; Nicolosi, V.; Nellist, P. D. Atomic Scale Dynamics of a Solid State Chemical Reaction Directly Determined by Annular Dark-Field Electron Microscopy. *Sci. Rep.* **2015**, *4*, No. 7555.
(18) Lu, P.; Yan, P.; Romero, E.; Spoerke, E. D.; Zhang, J.-G.; Wang, C.-M. Observation of Electron-Beam-Induced Phase Evolution Mimicking the Effect of the Charge−Discharge Cycle in Li-Rich Layered Cathode Materials Used for Li Ion Batteries. *Chem. Mater.* **2015**, *27*, 1375−1380.
(19) Ishikawa, R.; Mishra, R.; Lupini, A. R.; Findlay, S. D.; Taniguchi, T.; Pantelides, S. T.; Pennycook, S. J. Direct Observation of Dopant Atom Diffusion in a Bulk Semiconductor Crystal Enhanced by a Large Size Mismatch. *Phys. Rev. Lett.* **2014**, *113*, No. 155501.
(20) Lehtinen, O.; Kurasch, S.; Krasheninnikov, A. V.; Kaiser, U. Atomic Scale Study of the Life Cycle of a Dislocation in Graphene from Birth to Annihilation. *Nat. Commun.* **2013**, *4*, No. 2098.
(21) Kwon, B. J.; Yin, L.; Park, H.; Parajuli, P.; Kumar, K.; Kim, S.; Yang, M.; Murphy, M.; Zapol, P.; Liao, C.; Fister, T. T.; Klie, R. F.; Cabana, J.; Vaughey, J. T.; Lapidus, S. H.; Key, B. A High Voltage Mg-Ion Battery Cathode via a Solid Solution Cr−Mn Spinel Oxide. *Chem. Mater.* **2020**, *32*, 6577−6587.
(22) Allen, L. J.; Findlay, S. D.; et al. Modelling the Inelastic Scattering of Fast Electrons. *Ultramicroscopy* **2015**, *151*, 11−22.
(23) Hohenberg, P.; Kohn, W. Inhomogeneous Electron Gas. *Phys. Rev. B* **1964**, *136*, No. 864.
(24) Kresse, G.; Furthmüller, J. Efficient Iterative Schemes for Ab Initio Total-Energy Calculations Using a Plane-Wave Basis Set. *Phys. Rev. B* **1996**, *54*, No. 11169.
(25) Blöchl, P. E. Projector Augmented-Wave Method. *Phys. Rev. B* **1994**, *50*, No. 17953.
(26) Kresse, G.; Joubert, D. From Ultrasoft Pseudopotentials to the Projector Augmented-Wave Method. *Phys. Rev. B* **1999**, *59*, No. 1758.
(27) Perdew, J. P.; Burke, K.; Ernzerhof, M. Generalized Gradient Approximation Made Simple. *Phys. Rev. Lett.* **1996**, *77*, No. 3865.
(28) Henkelman, G.; Uberuaga, B. P.; Jónsson, H. A Climbing Image Nudged Elastic Band Method for Finding Saddle Points and Minimum Energy Paths. *J. Chem. Phys.* **2000**, *113*, 9901−9904.
(29) Pennycook, S. J.; Boatner, L. A. Chemically Sensitive Structure-Imaging with a Scanning Transmission Electron Microscope. *Nature* **1988**, *336*, 565.
(30) Wyckoff, R. W. G. *The Analytical Expression of the Results of the Theory of Space-Groups*; Carnegie institution of Washington, 1922; pp 39−46.
(31) Irani, K. S.; Sinha, A. P. B.; Biswas, A. B. Effect of Temperature on the Structure of Manganites. *J. Phys. Chem. Solids* **1962**, *23*, 711−727.
(32) Malavasi, L.; Ghigna, P.; Chiodelli, G.; Maggi, G.; Flor, G. Structural and Transport Properties of $Mg_{1-x}Mn_xMn_2O_{4\pm\delta}$ Spinels. *J. Solid State Chem.* **2002**, *166*, 171−176.
(33) Radhakrishnan, N. K.; Biswas, A. B. A Neutron Diffraction Study of the Cation Migration in $MgMn_2O_4$. *Phys. Status Solidi A* **1976**, *37*, 719−722.
(34) Grunes, L. A.; Leapman, R. D.; Wilker, C. N.; Hoffmann, R.; Kunz, A. B. Oxygen K Near-Edge Fine Structure: An Electron-Energy-Loss Investigation with Comparisons to New Theory for Selected 3d Transition-Metal Oxides. *Phys. Rev. B* **1982**, *25*, No. 7157.
(35) Abbate, M.; de Groot, F. M. F.; Fuggle, J. C.; Fujimori, A.; Strebel, O.; Lopez, F.; Domke, M.; Kaindl, G.; Sawatzky, G. A.; Takano, M.; et al. Controlled-Valence Properties of $La_{1-x}Sr_xFeO_3$ and $La_{1-x}Sr_xMnO_3$ Studied by Soft-x-Ray Absorption Spectroscopy. *Phys. Rev. B* **1992**, *46*, No. 4511.
(36) Laffont, L.; Gibot, P. High Resolution Electron Energy Loss Spectroscopy of Manganese Oxides: Application to Mn_3O_4 Nanoparticles. *Mater. Charact.* **2010**, *61*, 1268−1273.
(37) Varela, M.; Oxley, M. P.; Luo, W.; Tao, J.; Watanabe, M.; Lupini, A. R.; Pantelides, S. T.; Pennycook, S. J. Atomic-Resolution Imaging of Oxidation States in Manganites. *Phys. Rev. B* **2009**, *79*, No. 085117.
(38) Gilbert, B.; Frazer, B. H.; Belz, A.; Conrad, P. G.; Nealson, K. H.; Haskel, D.; Lang, J. C.; Srajer, G.; De Stasio, G. Multiple Scattering Calculations of Bonding and X-Ray Absorption Spectroscopy of Manganese Oxides. *J. Phys. Chem. A* **2003**, *107*, 2839−2847.
(39) Wang, Z. L.; Yin, J. S.; Jiang, Y. D. EELS Analysis of Cation Valence States and Oxygen Vacancies in Magnetic Oxides. *Micron* **2000**, *31*, 571−580.
(40) Tan, H.; Verbeeck, J.; Abakumov, A.; Van Tendeloo, G. Oxidation State and Chemical Shift Investigation in Transition Metal Oxides by EELS. *Ultramicroscopy* **2012**, *116*, 24−33.
(41) Zhang, S.; Livi, K. J. T.; Gaillot, A.-C.; Stone, A. T.; Veblen, D. R. Determination of Manganese Valence States in (Mn^{3+}, Mn^{4+}) Minerals by Electron Energy-Loss Spectroscopy. *Am. Mineral.* **2010**, *95*, 1741−1746.
(42) Schmid, H. K.; Mader, W. Oxidation States of Mn and Fe in Various Compound Oxide Systems. *Micron* **2006**, *37*, 426−432.
(43) Sai Gautam, G.; Canepa, P.; Urban, A.; Bo, S.-H.; Ceder, G. Influence of Inversion on Mg Mobility and Electrochemistry in Spinels. *Chem. Mater.* **2017**, *29*, 7918−7930.
(44) Jiang, N. Electron Beam Damage in Oxides: A Review. *Rep. Prog. Phys.* **2016**, *79*, No. 016501.
(45) San, X.; Zhang, B.; Wang, J.; Wu, B.; Ma, X. In Situ Tracking the Reversible Spinel-Rocksalt Structural Transformation between Mn_3O_4 and MnO. *Micron* **2017**, *92*, 13−18.
(46) Thornburg, D. D.; Wayman, C. M. Specimen Temperature Increases during Transmission Electron Microscopy. *Phys. Status Solidi A* **1973**, *15*, 449−453.
(47) Urban, A.; Lee, J.; Ceder, G. The Configurational Space of Rocksalt-type Oxides for High-capacity Lithium Battery Electrodes. *Adv. Energy Mater.* **2014**, *4*, No. 1400478.
(48) Reed, J.; Ceder, G.; Van Der Ven, A. Layered-to-Spinel Phase Transition in Li_xMnO_2. *Electrochem. Solid State Lett.* **2001**, *4*, A78.

https://dx.doi.org/10.1021/acs.chemmater.0c03121
Chem. Mater. 2020, 32, 10456−10462